Biomicrofluidics ARTICLE scitation.org/journal/bmf

Red blood cell recognition and posture estimation in microfluidic chip based on lensless imaging

Cite as: Biomicrofluidics **15**, 034109 (2021); doi: 10.1063/5.0050381
Submitted: 15 March 2021 · Accepted: 17 May 2021 ·
Published Online: 28 May 2021

View Online Export Citation CrossMark

Jianwei Li,[a] Li Dai, Ningmei Yu,[a] and Yinfeng Wu

AFFILIATIONS

Faculty of Automation and Information Engineering, Xi'an University of Technology, Xi'an 710048, China.

[a]**Authors to whom correspondence should be addressed:** lijw@xaut.edu.cn and yunm@xaut.edu.cn

ABSTRACT

On the one hand, lensless imaging technology has become one of the key technologies to achieve point-of-care testing; on the other hand, microfluidic technology has shown great application potential in the field of biological detection. Using mainstream lensless imaging technology to achieve biological cell imaging in microfluidic chips has technical limitations. In particular, it is more difficult to achieve lensless imaging for non-spherical cells in microfluidic chips such as red blood cells. Achieving red blood cell recognition and posture estimation in a microfluidic chip under the lensless imaging, combined with mainstream lensless imaging technology, can provide more effective red blood cell morphological parameters for medical diagnosis. In this paper, the method for red blood cell recognition and posture estimation in microfluidic chips based on lensless imaging is given. First, the relevant theoretical basis is introduced. Then, the models of red blood cell recognition and posture estimation in microfluidic chips based on lensless imaging are given. The effect of red blood cell flipping on lensless imaging is analyzed in the modeling process. Finally, the effectiveness of the proposed method is verified by experiments. Experiments show that the proposed method can well achieve red blood cell recognition and posture estimation through the shape characteristics of red blood cells.

Published under an exclusive license by AIP Publishing. https://doi.org/10.1063/5.0050381

I. INTRODUCTION

Complete blood count (CBC) is one of the common blood tests prescribed by doctors for clinical diagnosis and prognosis.[1] Today's CBC is no longer a simple function of counting red blood cells (RBCs), white blood cells (WBCs), and platelets (PLTs) but a comprehensive detection of blood cells. For example, in the International Council For Standardization in Haematology (ICSH) 2014 guidelines for the evaluation of blood cell analyzers, parameters related to RBC size, such as the RBC distribution width (RDW), are also established as a part of a CBC.[2] We believe that with the development of technology, more CBC parameters will be provided to help medical diagnosis.

Point-of-care testing (POCT) is defined as medical diagnostic testing at or near the point of care, that is, at the time and place of patient care.[3] How to achieve a CBC in POCT is very important, and it is also a research hotspot in recent years.[4–6] Currently, automatic hematology analyzers (AHAs) are extensively employed for CBC. The flow cytometer is the most representative equipment among AHAs. It is usually placed in centralized facilities and shared by many users due to their large size and significant cost for maintenance. It is not suitable for POCT.[7]

In recent years, with the development of microfluidics-based lab-on-a-chip (LOC) technology, a compact, low-cost, and easy-to-use AHA, which is suitable for POCT, has become possible.[8–11] This technology relies on traditional microscopes as imaging systems, which greatly increases equipment costs and limits equipment portability.[12] The maturity of lensless imaging systems has brought hope to replace traditional microscopes in LOC technology.[13,14] Figure 1 shows a typical lensless imaging system. An RBC is placed directly on a CMOS image sensor (CIS), and a diffraction image of the RBC is formed on the CIS.[15–17]

The research hotspot of lensless imaging is how to obtain the information of the observed object through diffraction image. The existing diffraction image processing technology mainly has two technical routes: one is the lensless microscope technology based on holographic reconstruction,[18–20] and the other is the cytometer technology based on diffraction fringes to obtain cell characteristics.[21–25] For the extremely low resolution of lensless imaging, both technologies present great challenges. Particularly, when the microfluidic chip is introduced, the imaging of moving cells will bring further difficulties.

Published under an exclusive license by AIP Publishing

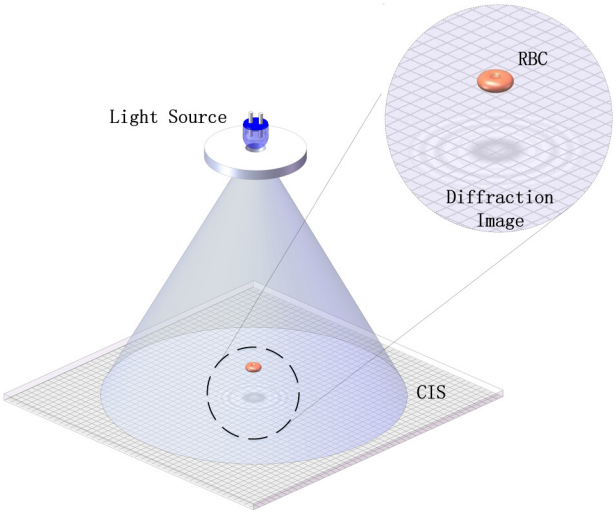

FIG. 1. Typical lensless imaging system. An RBC is placed directly on a CIS, and only a diffraction image of RBCs can be formed on the CIS.

When biological cells move in a microfluidic chip, the cells will flip, which has a great impact on the image processing of lensless imaging. The longitudinal resolution of the holographic reconstruction technology is much smaller than the lateral resolution,[26] and it is difficult to deal with measurement errors caused by cell flipping. The cytometer technology based on diffraction fringes can only obtain lateral edge information,[22,23] not to mention the problem of cell flipping. Particularly for non-spherical cells like RBCs, their three-dimensional morphology is of great significance for medical diagnosis. RBCs are typically shaped as biconcave disks, but due to diseases, some RBC morphologies will change. For example, abnormal RBC morphology has been one of the important diagnostic basis for anemia.[27] Particularly, under the condition of lensless imaging, hereditary RBC membrane disorders[28–31] such as hereditary spherocytosis need to be diagnosed through the three-dimensional morphology of RBCs. By determining the RBC posture, and obtaining the diffraction image in this posture, the morphological information of RBCs in a specific posture can be obtained, which is an advantage that the planar lensless imaging does not have. Therefore, under the condition of lensless imaging, in a microfluidic chip, identifying the RBCs and determining the posture of the RBCs have important research significance. It can be combined with the existing diffraction image processing technology to more effectively determine the morphological parameters of RBCs.

In this paper, the relevant theoretical basis is introduced at first. Then, the models of RBC recognition and posture estimation in a microfluidic chip based on lensless imaging are given. The effect of RBC flipping on lensless imaging is analyzed in the modeling process. At last, the effectiveness of the proposed method is verified by experiments. Experiments show that the proposed method can well achieve RBC recognition and posture estimation through the shape characteristics of RBCs.

II. THEORETICAL FRAMEWORK

To make the proposed method suitable for POCT, we use the relationship between the RBC edge and the diffraction pattern to build a model to realize the recognition and pose estimation of the RBC. Generally, in a typical lensless imaging system, the distance between the cell and the imaging plane is approximately hundreds of micrometers to millimeters. The light source generally adopts a monochromatic visible light source, and its light wavelength is approximately several hundreds of nanometers. According to diffraction theory, the spectral linewidth of the diffraction pattern of a RBC is larger than the diameter of the RBC, so the diffraction pattern is the result of the multi-position diffraction superposition.[22,23] The shape of RBCs is not a perfect circle or a regular ellipse. As a result, we can only use single-edge diffraction theory instead of circle or ellipse diffraction theory for modeling.

A. Fresnel diffraction at a straight edge

As shown in Fig. 2, P_0 is a monochromatic point light source. P is an imaging point on an image plane. O is the origin of coordinates, and (ξ, η) is the coordinate of the point Q on the small hole. r and s are the distances from the origin of the coordinates to points P_0 and P, respectively. r' and s' are the distances from Q to points P_0 and P, respectively. Based on the Fresnel–Kirchhoff diffraction integral, if the conditions shown in (1) are true, the Fresnel–Kirchhoff diffraction can be approximated as Fraunhofer diffraction; otherwise, it can only be approximated as Fresnel diffraction,[32]

$$|r'| \gg \frac{(\xi^2+\eta^2)_{\max}}{\lambda} \text{ and } |s'| \gg \frac{(\xi^2+\eta^2)_{\max}}{\lambda}, \tag{1}$$

where λ is the optical wavelength.

Both theory and practice have proved that the Fresnel diffraction at a straight edge can well describe the relationship between the position of the diffraction edge and the intensity of the diffraction fringe.[22,23] If the diffraction occurs on a semi-infinite plane bounded by a sharp straight edge, the light intensity at the imaging

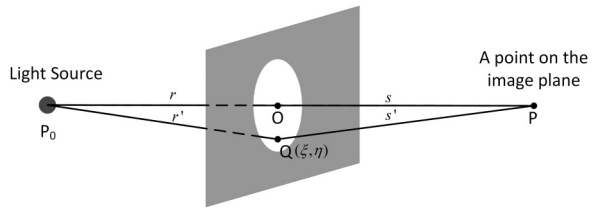

FIG. 2. Fresnel–Kirchhoff diffraction. P_0 is a monochromatic point light source. P is an imaging point on an image plane. O is the origin of coordinates, and (ξ, η) is the coordinate of the point Q on the small hole. r and s are the distances from the origin of the coordinates to points P_0 and P, respectively. r' and s' are the distances from Q to points P_0 and P, respectively.

Published under an exclusive license by AIP Publishing

plane can be expressed as[32]

$$I_{str} = \frac{1}{2}\left\{\left[\frac{1}{2} + C(w)\right]^2 + \left[\frac{1}{2} + S(w)\right]^2\right\} I_0, \tag{2}$$

where I_0 is average light intensity and $C(w)$ and $S(w)$ are known as Fresnel's integrals, which can be expressed as

$$\left.\begin{aligned} C(w) &= \int_0^w \cos\left(\frac{\pi}{2}\tau^2\right) d\tau, \\ S(w) &= \int_0^w \sin\left(\frac{\pi}{2}\tau^2\right) d\tau, \end{aligned}\right\} \tag{3}$$

and w can be expressed as

$$w = \sqrt{\frac{2}{\lambda}\left(\frac{1}{r'} + \frac{1}{s'}\right)} x. \tag{4}$$

B. Diffracted light intensity model at an arc edge

According to the Huygens–Fresnel principle, every point of a wave-front may be considered a center of a secondary disturbance, which gives rise to spherical wavelets. The wave-front at any later instant may be regarded as the envelope of these wavelets, and the secondary wavelets mutually interfere.[32] If the diffraction of an arbitrary point on an arc edge can be regarded as the diffraction on the tangent line of that point, the Fresnel diffraction at a straight edge can well describe the relative positional relationship between the arc edge and the diffraction fringe. Every point of a wave-front may be considered as a center of a secondary disturbance, which gives rise to spherical wavelets. There is no significant difference in the secondary wavelets mutually interfere of the straight edge diffraction and the arc edge diffraction. That is, using the straight edge diffraction theory approximation will not significantly change the position information of the diffraction fringe to the arc edge.[22,23] But for the diffracted light intensity, an arc edge diffraction has a larger diffusion space, so the diffracted light intensity has a greater attenuation than the diffracted light intensity at a straight edge.

Therefore, based on the Fresnel diffraction at a straight edge, the intensity distribution considering the amplitude attenuation can be expressed as

$$I_{arc} = \alpha I_{str} + (1 - \alpha) I_0, \tag{5}$$

where α is the attenuation coefficient. According to the difference in the integral area of the arc edge diffracted light intensity and the straight edge diffracted light intensity, we can get

$$\int_0^{2\pi(R_{arc}+x)} I_{arc}(x) dl = \int_0^{2\pi R_{arc}} I(x) dl, \tag{6}$$

where R_{arc} is the radius of the arc edge and x is the distance from the center of the arc. So, the attenuation coefficient α can be expressed as

$$\alpha = \frac{I_{arc} - I_0}{I - I_0} = \frac{R_{arc}}{x}. \tag{7}$$

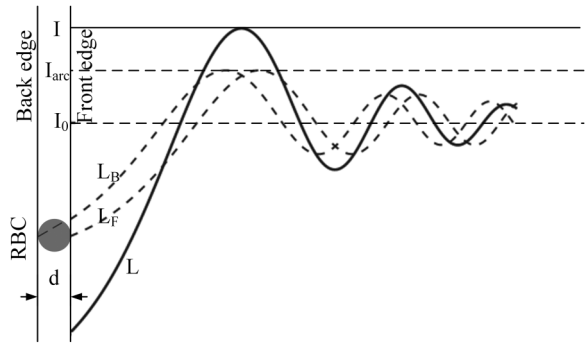

FIG. 3. Schematic diagram of diffraction intensity curve superposition of an RBC. The distance between the two positions where the diffraction superposition occurs is d, which is also the diameter of the RBC. L_F and L_B are the diffraction light intensity curves produced by the front edge and the back edge, respectively. L is the light intensity curve after superposition.

C. Effects of superposition of diffraction fringes

Under typical lensless imaging conditions, the radius of the first bright ring of the RBC diffraction pattern is approximately 10–20 μm, while the radius of the RBC is approximately 3–4 μm. Therefore, the RBC diffraction pattern must be the multi-position diffraction superposition.

Figure 3 is a schematic diagram of diffraction intensity curve superposition of an RBC. The distance between the two positions where the diffraction superposition occurs is d, which is also the diameter of the RBC. L_F and L_B are the diffraction light intensity curves produced by the front edge and the back edge, respectively. L is the light intensity curve after superposition. It is clear that the superposition of the diffraction of the two arc edges is conditional. The condition is that the tangents of the two diffraction points must be parallel, and their normals must coincide.

According to the size characteristics of RBCs, we only discuss the case where the first peak of L is generated by the superposition of the first peaks of L_F and L_B. I is the light intensity of the first peak of the curve L, which has two clear characteristics: one is that as the arc edge distance d increases, I will decrease; the other is that as the arc edge radius increases, I will increase. These two characteristics are very important for RBC recognition and posture estimation.

III. RBC POSTURE MODELING

The Fresnel–Kirchhoff diffraction formula can describe the formation mechanism of diffraction very well. As shown in Fig. 2, a point source P_0, which considers a monochromatic wave, propagates through an opening in a plane opaque screen. The total

Published under an exclusive license by AIP Publishing

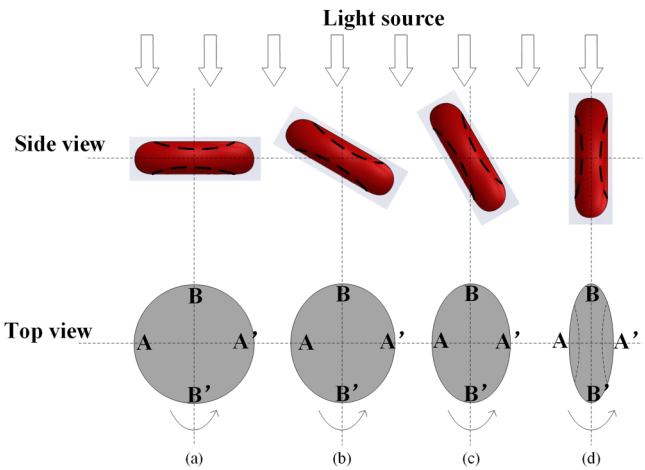

FIG. 4. Schematic diagram of flipped RBC modeling. (a) RBC is parallel to the imaging surface. (b) RBC is inclined to the imaging surface at a small angle. (c) RBC is inclined to the imaging surface at a large angle. (d) RBC is perpendicular to the imaging surface. The top view can be considered an edge model that produces diffraction. A and A′ are the saddle-points not affected by the flip. B and B′ are the saddle-points affected by the flip.

disturbance at P, which is the light disturbance to be determined, is given by[32]

$$U(P) = -\frac{\mathrm{i}\cos\delta}{\lambda}\frac{A\mathrm{e}^{\mathrm{i}k(r'+s')}}{r's'}\iint_A \mathrm{e}^{\mathrm{i}kf(\xi,\eta)}\mathrm{d}\xi\mathrm{d}\eta, \tag{8}$$

where δ is the angle between the line P_0P and the normal to the screen. Based on the principle of the method of stationary phase,[32] as the point (ξ, η) explores the domain of integration, the function $f(\xi, \eta)$ will change by very many wavelengths, so that both the real and imaginary parts of the integrand will change sign many times. In consequence, the contributions from the various elements will in general virtually cancel each other out (destructive interference). The situation is, however, different for an element, which surrounds a point (called critical point or pole) where $f(\xi, \eta)$ is stationary. Here, the integrand varies much more slowly and may be expected to give a significant contribution. The intensity distribution of the diffraction pattern depends on choosing a path of integration in such a way that the integrand, by virtue of its exponential factor, contributes negligibly to the integral except in the vicinity of certain critical points, these being either saddle-points or end points of the path of integration.

As show in Fig. 4, a flipped RBC model is described, and the top view can also be considered an edge model that produces diffraction. There are two typical situations in the saddle-point formation of the diffraction integral path. One is the saddle-point affected by the flip, such as B and B′, and the other is the saddle-point not affected by the flip, such as A and A′. Obviously, due to flipping at points B and B′, the saddle-point disturbance will increase.

Figures 5(a) and 5(b) correspond to the schematic diagrams of the light intensity distribution of the first bright ring of the RBC diffraction pattern without considering the effect of flipping on the saddle-points and considering the effect of flipping on the saddle-points, respectively. Curves (a)–(d) correspond to the four postures in Fig. 4. Without considering the effect of flipping on the saddle-points, the light intensity distribution of the first bright ring of the diffraction pattern depends on the arc edge radius. When considering the effect of flipping on the saddle-points, for the flipping to introduce additional disturbances at the saddle-points B and B′, the diffracted light intensity of these points will decrease sharply. Since the shape of the RBCs is a biconcave disk, in posture (d), the saddle-points at positions A and A′ will disappear, and the light intensity will decrease sharply.

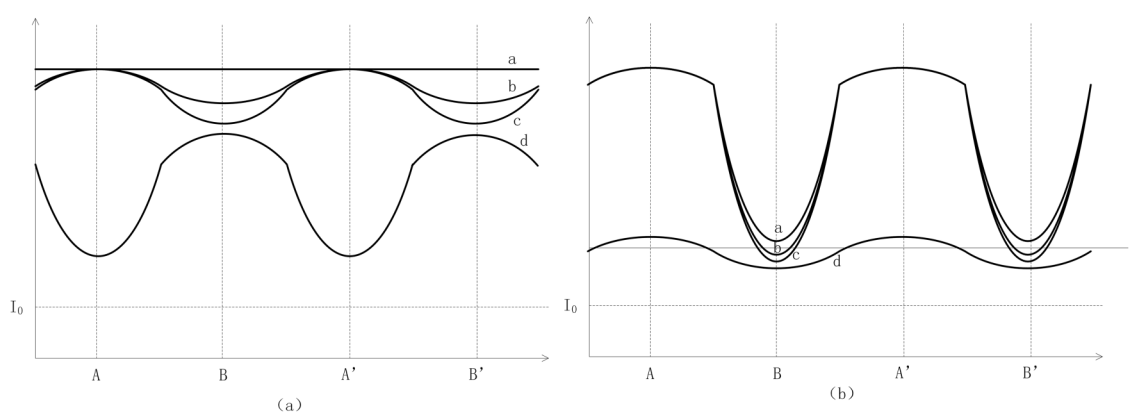

FIG. 5. (a) Schematic diagram of the light intensity distribution of the first bright ring of an RBC without considering the effect of flipping on the saddle-points. (b) Schematic diagram of the light intensity distribution of the first bright ring of an RBC considering the effect of flipping on the saddle-points. Experiments prove that (b) is in line with the actual situation.

Published under an exclusive license by AIP Publishing

IV. MODEL VERIFICATION AND USAGE

A. Experimental system

As shown in Fig. 6, the system consists of two subsystems, namely, the imaging subsystem and the image processing subsystem. Figure 6(a) is the imaging subsystem. It includes a light source and a CIS. To avoid the influence of ambient light, they are placed in a dark room. The size of the imaging subsystem is approximately 5 * 5 * 11 cm. To simplify the calculation, a parallel light source is used in the experiment, as shown in Fig. 6(c). It uses a monochromatic point light source and a convex lens to obtain the parallel light. Figure 6(d) is an imaging module. A CIS model MT9P031 is used. The resolution is 1944 * 2592 and the pixel size is 2.2 μm. Figure 6(e) shows a microfluidic chip placed on the CIS in the experiment. The microfluidic chip used in the experiment is shown in Fig. 6(f), with three inlets and one outlet. The inlet in the middle is used to input the sample, and the inlets on both sides are used to input the sheath fluid. To have better portability of the system, an embedded computer is used for an image processing subsystem, as shown in Fig. 6(b). The embedded computer is composed of an ARM Cortex-A53 eight-core processor, 2GB DDR3 SDRAM, 32GB flash memory, and 7-in. LCD screen.

B. Robustness verification of light intensity model

The diffracted light intensity model at an arc edge is used to achieve the RBC recognition and posture estimation in microfluidic chip based on lensless imaging. The degree of dependence of the light intensity model on the stability of the light source intensity directly affects the robustness of the algorithm. Therefore, we first verify the influence of light intensity on the model.

As shown in Fig. 7, the monodisperse polystyrene microspheres of 6 and 7 μm are imaged by a lensless imaging system under non-uniform light intensity. The light intensity of the first bright ring of the diffraction pattern of the microspheres is used to verify the validity and robustness of the diffracted light intensity model at an arc edge. Figure 8 shows the absolute brightness of the

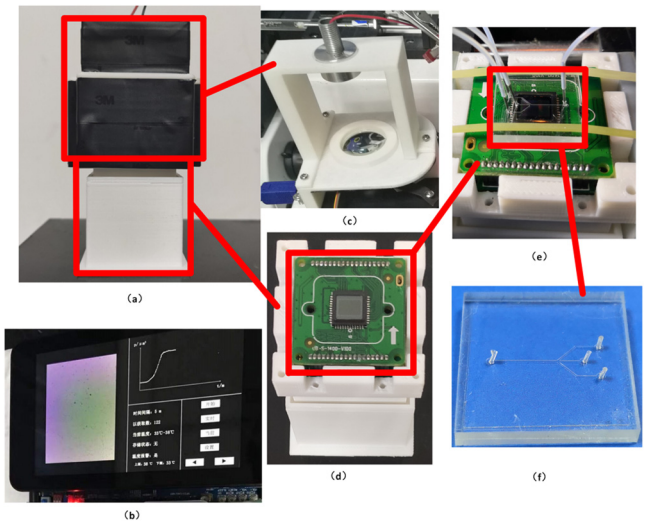

FIG. 6. The experiment system. (a) is the imaging subsystem. It includes a light source and a CIS. To avoid the influence of ambient light, they are placed in a dark room. (b) is an embedded computer is used for image processing subsystem. (c) is a device for obtaining parallel light sources. (d) is the imaging module. A CIS model MT9P031 is used. The resolution is 1944 * 2592 and the pixel size is 2.2 μm. (e) shows a microfluidic chip placed on the CIS in the experiment. (f) is the microfluidic chip used in the experiment, which has three inlets and one outlet. The inlet in the middle is used to input the sample, and the inlets on both sides are used to input the sheath fluid.

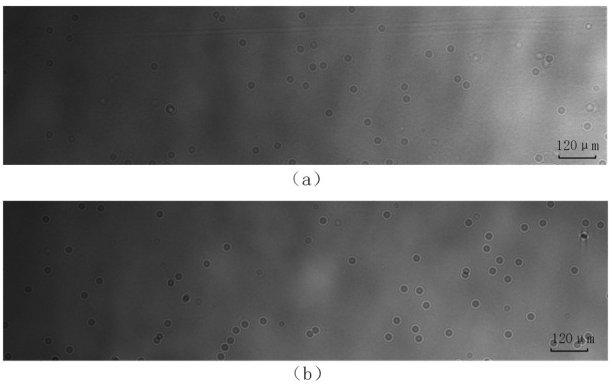

FIG. 7. Partial view of lensless imaging of microspheres under non-uniform light source. The light intensity of the first bright ring of the diffraction pattern of the microspheres can be used to verify the validity and robustness of the diffracted light intensity model at an arc edge. (a) 6 μm microspheres; (b) 7 μm microspheres.

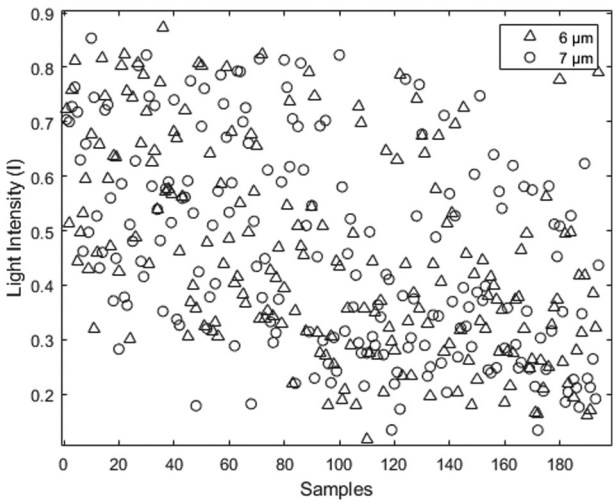

FIG. 8. The absolute brightness of the first bright ring of the diffraction pattern of 6 and 7 μm microspheres. Due to the non-uniform light source, the brightness of the first bright light ring of the diffraction pattern is distributed in almost the entire brightness range, regardless of whether the microspheres are 6 or 7 μm.

Published under an exclusive license by AIP Publishing

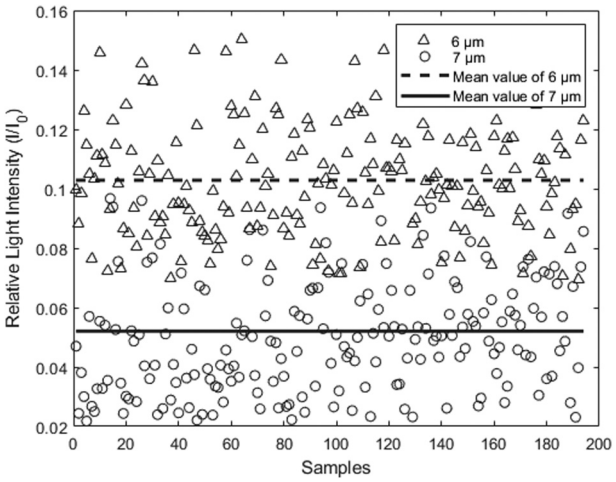

FIG. 9. The relative brightness of the first bright ring of the diffraction pattern of 6 and 7 μm microspheres. For the relative light intensity is used, it is easy to distinguish between 6 and 7 μm microspheres by the brightness of the first bright ring of the diffraction pattern.

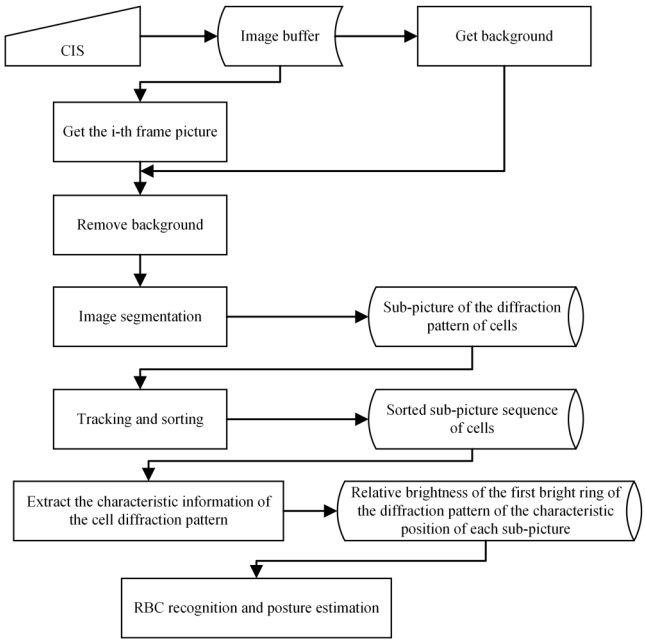

FIG. 10. The image processing flow for RBC recognition and posture estimation. It includes (1) remove background; (2) image segmentation; (3) tracking and sorting; (4) extract the characteristic information of the cell diffraction pattern; and (5) RBC recognition and posture estimation.

first bright ring of the diffraction pattern of 6 and 7 μm microspheres. Due to the non-uniform light source, the brightness of the first bright light ring of the diffraction pattern is distributed in almost the entire brightness range, regardless of whether the microspheres are 6 or 7 μm. Correspondingly, as shown in Fig. 9, if the relative light intensity is used, it is easy to distinguish between 6 and 7 μm microspheres by the brightness of the first bright ring of the diffraction pattern. It shows that the diffracted light intensity model at an arc edge of is valid. The result of the model is independent of the intensity of the light source, indicating that the model has good robustness.

It should be noted that according to the diffracted light intensity model at an arc edge, the brightness of the first bright ring of 7 μm microspheres should be greater than that of 6 μm microspheres. This is inconsistent with what is shown in Fig. 9. In fact, this reflects the effect of the superposition of diffraction fringes. This conclusion can be easily verified by the superposition of two arc-side diffraction.

C. RBC recognition and posture estimation

As shown in Fig. 6(f), to realize RBC recognition and posture estimation, we used a microfluidic chip made of polydimethylsiloxane (PDMS) with three inlets and one outlet as the microchannel. The width of the microchannel is ~250 μm. The flow rate of the sheath fluid at the inlets on both sides is ~1.2 μl/min, and the flow rate of the RBC sample at the middle inlet is ~0.7 μl/min. The dilution ratio of the RBC sample is ~1:50 000. Under this experimental condition, the average throughput of cells is ~7 cells per second. The CIS collects images at 60 frames per second.

Figure 10 shows the Image processing flow for the RBC recognition and posture estimation. It includes the following steps: (1) Remove background. First, we need to cache several pictures to obtain a clean background picture and then make a difference to obtain a cell diffraction image without background; (2) Image segmentation. Find the diffraction pattern of the cells in each frame of image and segment them into sub-pictures; (3) Tracking and sorting. Track the diffraction pattern of the same cell in each frame of image and sort them; (4) Extract the characteristic information of the cell diffraction pattern. We need to obtain the relative brightness of the first bright ring of the diffraction pattern of the characteristic position of each sub-picture, which can be used for red blood cell recognition and pose estimation; (5) RBC recognition and posture estimation. Under current conditions, the image processing flow can realize real-time processing, which means that each frame of image can be processed within 1/60 s.

The diffraction patterns in Fig. 11 are the diffraction images of five randomly selected RBCs obtained every 15 frames and k is the start frame. The common feature of these diffraction patterns is that the first bright ring has two light intensity minimum points in the approximate x axis direction and two light intensity maximum points in the approximate y axis direction. According to the previous analysis, we know that the two minimum light intensity points are caused by RBC flipping. The two maximum light intensity points should conform to the diffraction light intensity model at an arc edge considering the influence of diffraction superposition. Obviously, this light intensity characteristic of the first bright ring of the diffraction pattern is caused by the dish-shaped structure of RBCs, which can be used for RBC recognition. Figure 12 shows the

Published under an exclusive license by AIP Publishing

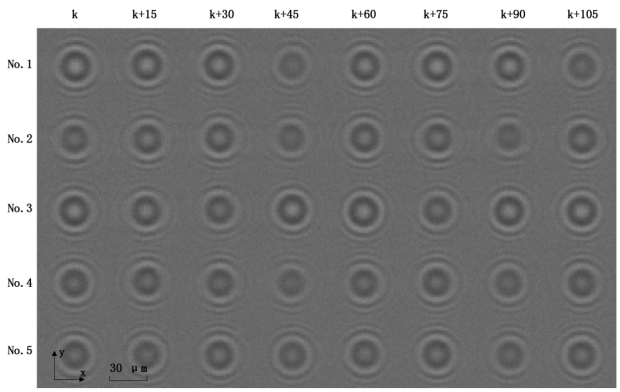

FIG. 11. Lensless imaging of RBCs at different times in a microfluidic chip. The diffraction patterns are the diffraction images of five randomly selected RBCs obtained every 15 frames. The common feature of these diffraction patterns is that the first bright ring has two light intensity minimum points in the approximate *x* axis direction, and two light intensity maximum points in the approximate *y* axis direction.

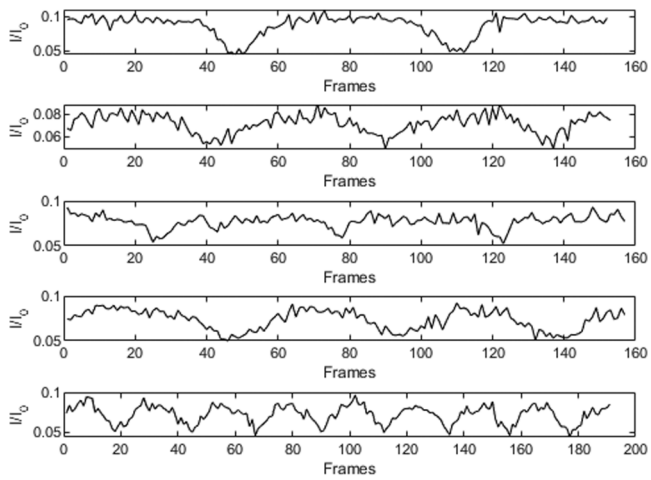

FIG. 13. The light intensity fluctuation at the maximum point of the first bright ring of the diffraction pattern caused by the flipping of RBCs. Between every two minimum values, the RBCs have flipped 180°.

light intensity distribution of the first bright ring of the diffraction pattern of No. 1 RBC at different times.

As shown in Fig. 4, since the shape of the RBCs is a biconcave disk, in posture (d), the saddle-points at positions A and A′ will disappear, and the light intensity will decrease sharply. A and A′ correspond to the maximum light intensity points of the first bright ring of the diffraction pattern. Therefore, when the maximum light intensity of the first bright ring decreases sharply, it indicates that the RBC disk surface is parallel to the direction of the light source. This feature can be used for RBC posture estimation.

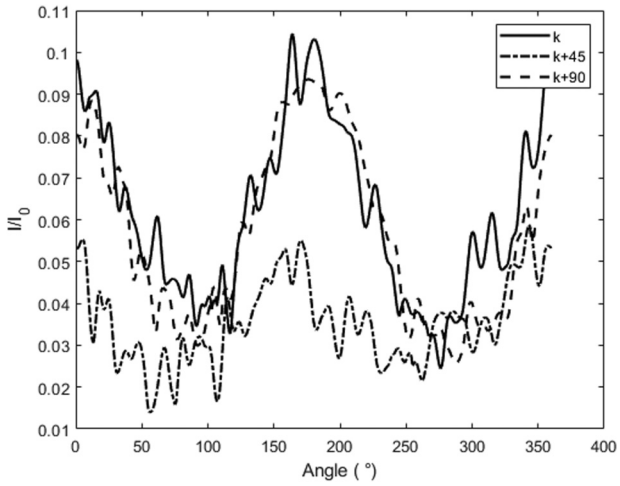

FIG. 12. Light intensity distribution of the first bright ring of the diffraction pattern of No. 1 RBC at different times. Curve k + 45 represents the situation where the RBC disk surface and the light source are approximately parallel, and the maximum value of the light intensity decreases sharply.

As shown in Fig. 12, Curve k + 45 represents the situation where the RBC disk surface and the light source are approximately parallel, and the maximum value of the light intensity decreases sharply. Figure 13 shows the dynamic change of the maximum brightness of the first bright ring of the diffraction pattern as the RBCs are flipped in the microfluidic chip. Obviously, between every two minimum values, the RBCs have flipped 180°.

The frame numbers corresponding to the two minimum light intensity values are k_1 and k_2, and $k_2 > k_1$. If the position of the RBC dish surface parallel to the light source direction is defined as the initial position, the flip angle of the RBC in the *i*th frame is

$$\beta_i = \frac{180}{k_2 - k_1}(i - k_1). \tag{9}$$

For the extremely low resolution of lensless imaging, noise has a great influence on the image quality. Therefore, in practice, it is necessary to perform a filtering operation on the data shown in Fig. 13 to reduce the influence of noise and improve the accuracy of k_1 and k_2. It is clear that increasing the image frame rate and reducing the RBC flip speed can improve the measurement accuracy of the flip angle.

V. CONCLUSION

The proposed method can well achieve RBC recognition and posture estimation through the shape characteristics of RBCs. It can make up for the shortcomings of the existing mainstream lensless imaging technology in RBC imaging in the microfluidic chip. Since the RBCs in the microfluidic chip are flipped, only obtaining the planar image of the biconcave disk RBCs cannot fully characterize the RBC morphology. This paper points out for the first time

Published under an exclusive license by AIP Publishing

that the light intensity of the diffraction fringe of the lensless imaging of the RBCs in the microfluidic chip is affected by the RBC flipping, rather than the simple lensless imaging of the RBCs in a static posture. Combining the characteristics of the shape of RBCs, this paper presents a method of RBC recognition in a microfluidic chip under lensless imaging and also gives the posture estimation algorithm of the RBCs in the microfluidic chip at any time. All of these are proved to be effective through experiments.

ACKNOWLEDGMENTS

This work was supported by the National Natural Science Foundation of China (Nos. 61771388 and 61471296).

DATA AVAILABILITY

The data that support the findings of this study are available from the corresponding authors upon reasonable request.

REFERENCES

[1]R. Agarwal, A. Sarkar, A. Bhowmik, D. Mukherjee, and S. Chakraborty, Biosens. Bioelectron. **150**, 111935 (2020).
[2]C. Briggs, N. Culp, B. Davis, G. d'Onofrio, G. Zini, and S. J. Machin, Int. J. Lab. Hematol. **36**, 613 (2014).
[3]Y. H. Ghallab and Y. Ismail, IEEE Circuits Syst. Mag. **14**, 27 (2014).
[4]V. Laxmi, S. Tripathi, and A. Agrawal, in *Mechanical Sciences*, edited by U. S. Dixit and S. K. Dwivedy (Springer, Singapore, 2021), p. 169.
[5]P. B. Luppa and R. Junker, in *Point-of-Care Testing: Principles and Clinical Applications*, edited by P. B. Luppa and R. Junker (Springer, Berlin, 2018).
[6]U. A. Gurkan, S. Moon, H. Geckil, F. Xu, S. Wang, T. J. Lu, and U. Demirci, Biotechnol. J. **6**, 138 (2011).
[7]S. H. Cho, J. M. Godin, C.-H. Chen, W. Qiao, H. Lee, and Y.-H. Lo, Biomicrofluidics **4**, 43001 (2010).
[8]X. Dong, P. Song, and X. Liu, IEEE Trans. Nanobiosci. **18**, 373 (2019).
[9]J. Lee, M. Nolan, and H. Lee, IEEE Trans. Nanobiosci. **18**, 240 (2019).
[10]S. F. Jackson and D. C. Cole, Global J. Health Sci. **5**, 54 (2013).
[11]P. Yager, T. Edwards, E. Fu, K. Helton, K. Nelson, M. R. Tam, and B. H. Weigl, Nature **442**, 412 (2006).
[12]X. Huang, H. Yu, X. Liu, Y. Jiang, and M. Yan, IEEE Des. Test **32**, 32 (2015).
[13]X. Huang, Y. Jiang, H. Xu, X. Liu, H. W. Hou, M. Yan, and H. Yu, "A convolutional neural network based single-frame super-resolution for lensless blood cell counting," in *2016 IEEE Biomedical Circuits and Systems Conference (BioCAS)* (IEEE, 2016), p. 168.
[14]A. K. Mudraboyina, L. Blockstein, C. C. Luk, N. I. Syed, and O. Yadid-Pecht, IEEE Photonics J. **6**, 1 (2014).
[15]Z. Göröcs and A. Ozcan, IEEE Rev. Biomed. Eng. **6**, 29 (2013).
[16]X. Heng, D. Erickson, L. R. Baugh, Z. Yaqoob, P. W. Sternberg, D. Psaltis, and C. Yang, Lab Chip **6**, 1274 (2006).
[17]A. Ozcan and E. McLeod, Annu. Rev. Biomed. Eng. **18**, 77 (2016).
[18]A. Greenbaum, N. Akbari, A. Feizi, W. Luo, and A. Ozcan, PLoS One **8**, e76475 (2013).
[19]S. V. Kesavan, F. P. Navarro, M. Menneteau, F. Mittler, B. David-Watine, N. Dubrulle, S. L. Shorte, B. Chalmond, J.-M. Dinten, and C. P. Allier, J. Biomed. Opt. **19**, 36004 (2014).
[20]E. McLeod, T. U. Dincer, M. Veli, Y. N. Ertas, C. Nguyen, W. Luo, A. Greenbaum, A. Feizi, and A. Ozcan, ACS Nano **9**, 3265 (2015).
[21]G. Kim, Y. Jo, H. Cho, H.-S. Min, and Y. Park, Biosens. Bioelectron. **123**, 69 (2019).
[22]J. Li, L. Dai, N. Yu, Z. Li, and S. Li, Biotechnol. Appl. Biochem. (published online 2020).
[23]J. Li, L. Dai, N. Yu, Z. Li, and S. Li, Meas. Sci. Technol. **32**, 25701 (2021).
[24]M. Roy, G. Jin, D. Seo, M.-H. Nam, and S. Seo, Sens. Actuators B **201**, 321 (2014).
[25]M. Roy, D. Seo, C.-H. Oh, M.-H. Nam, Y. J. Kim, and S. Seo, Biosens. Bioelectron. **67**, 715 (2015).
[26]C. Zuo, J. Sun, J. Zhang, Y. Hu, and Q. Chen, Opt. Express **23**, 14314 (2015).
[27]K. Kaushansky, *Williams Hematology*, 9th ed. (McGraw-Hill, New York, 2016).
[28]M. Risinger and T. A. Kalfa, Blood **136**, 1250 (2020).
[29]T. A. More, B. Dalal, R. Devendra, P. Warang, A. Shankarkumar, and P. Kedar, Cytom. Part B Clin. Cytom. **98**, 238 (2020).
[30]L. Da Costa, J. Galimand, O. Fenneteau, and N. Mohandas, Blood Rev. **27**, 167 (2013).
[31]J. Delaunay, Blood Rev. **21**, 1 (2007).
[32]M. Born E. Wolf *et al.*, *Principles of Optics: Electromagnetic Theory of Propagation, Interference and Diffraction of Light*, 7th (expanded) ed. (Cambridge University Press, Cambridge, 1999).

Published under an exclusive license by AIP Publishing